RESEARCH ARTICLE
SOLID EARTH: SEISMOLOGY

Earth and Planetary Physics
8: 621–631, 2024
doi: 10.26464/epp2024034

No basalt accumulation and segregation atop the 660-km discontinuity beneath the Sea of Okhotsk

BingXin Zhou, and XiaoBo He*

Marine Science and Technology College, Zhejiang Ocean University, Zhoushan Zhejiang 316022, China

Key Points:

- No basalt accumulation is evident atop the 660-km discontinuity beneath the Sea of Okhotsk.
- Temperature and water content influence the regional topography of the 660-km discontinuity.
- The basalt accumulation at the base of the MTZ is sporadic, not ubiquitous.

Citation: Zhou, B. X., and He, X. B. (2024). No basalt accumulation and segregation atop the 660-km discontinuity beneath the Sea of Okhotsk. *Earth Planet. Phys.*, *8*(4), 621–631. http://doi.org/10.26464/epp2024034

Abstract: Recent seismic evidence shows that basalt accumulation is widespread in the mantle transition zone (MTZ), yet its ubiquity or sporadic nature remains uncertain. To investigate this phenomenon further, we characterized the velocity structure across the 660-km discontinuity that separates the upper mantle from the lower mantle beneath the Sea of Okhotsk by modeling the waveform of the S660P phase, a downgoing S wave converting into a P wave at the 660-km interface. These waves were excited by two regional >410-km-deep events and were recorded by stations in central Asia. Our findings showed no need to introduce velocity anomalies at the base of the MTZ to explain the S660P waveforms because the IASP91 model adequately reproduced the waveforms. This finding indicates that the basalt accumulation has not affected the bottom of the MTZ in the study area. Instead, this discontinuity is primarily controlled by temperature or water content variations, or both. Thus, we argue that the basalt accumulation at the base of the MTZ is sporadic, not ubiquitous, reflecting its heterogeneous distribution.

Keywords: 660-km discontinuity; S660P; basalt segregation; mantle transition zone; western Pacific subduction zone

1. Introduction

Two prominent discontinuities exist in the Earth's interior at depths of approximately 410 km and 660 km, representing transition boundaries of phase change primarily associated with the mineral olivine, a predominant constituent in the upper mantle (e.g., Helffrich and Wood, 2001). The mantle region between the two boundaries is the mantle transition zone (MTZ), a critical link connecting the upper and lower mantle (e.g., Bina, 1991). The structure of the MTZ is of great importance in gaining insights into the composition of the Earth's interior and the dynamics of the downgoing slab and upwelling plume (e.g., Morgan and Shearer, 1993; Shearer, 1995; Hu JS et al., 2018; Papanagnou et al., 2023).

It has long been recognized that temperature (e.g., Shearer, 1995) and water content (e.g., Litasov et al., 2005) primarily influence the depth of the mantle discontinuities in the MTZ. For instance, the arrival of slabs and plumes significantly changes the thickness of the MTZ (e.g., Foulger, 2012). The water content also affects the sharpness of upper mantle discontinuities (Wood, 1995; Smyth and Frost, 2002). In contrast, the velocity and density structures are mainly controlled by the composition of the MTZ (Wang JC et al., 2023). For instance, the accumulation of basalts at the MTZ significantly affects the composition, and thereby the velocity structure, of the MTZ (e.g., Kono et al., 2012; Goes et al., 2022).

The seismological evidence has increasingly suggested that the MTZ is rich in basalts, which result from the segregation of subducted oceanic slabs (Shen Y and Blum, 2003; Shen XZ et al., 2014; Taylor et al., 2019; Feng JK et al., 2021; Bissig et al., 2022; Tauzin et al., 2022; Yu CQ et al., 2023). However, whether the basalt accumulation at the base of the MTZ is ubiquitous or sporadic remains uncertain. Therefore, this study aimed to examine the ubiquity of the basalt accumulation by constraining the velocity structure across the 660-km discontinuity beneath the Sea of Okhotsk. We found no evidence of basalt accumulation at the base of the MTZ in this locality. Our finding sheds light on the nature of the composition and temperature in the study area and argues for sporadic, rather than ubiquitous, basalt accumulation at the base of the MTZ.

2. Data and Analysis

2.1 Data and Processing

In this study, waveform data of two deep-focus earthquakes (Table 1) were collected in the Kuril subduction zone recorded by central Asian stations (Tables 2 and 3). The distribution of earth-

Correspondence to: X. B. He, xiaobo.he@zjou.edu.cn
Received 21 APR 2024; Accepted 14 MAY 2024.
First Published online 14 JUN 2024.
©2024 by Earth and Planetary Physics.

Table 1. Information on the two earthquakes used in this study, taken from the U.S. Geological Survey catalog, in which the focal depths have been reconstrained by considering differential travel times between P and pP (Figure 2).

Date of earthquake	Latitude (°N)	Longitude (°E)	Focal depth (km)
July 23, 2016	47.58	146.94	419
November 2, 2018	47.83	146.70	440

Table 2. Information on the stations selected for the 2016 earthquake and the SdP conversion points at the 660-km discontinuity.

Network code	Station code	Latitude (°N)	Longitude (°E)	Conversion point latitude (°N)	Conversion point longitude (°E)
KR	MNAS	42.49	72.51	48.19	145.42
KZ	BRVK	53.06	70.28	48.40	145.52
KZ	KKAR	43.10	70.51	48.21	145.45
KZ	KUR01	50.72	78.56	48.33	145.39
KZ	KUR03	50.68	78.55	48.33	145.39
KZ	KUR05	50.64	78.54	48.33	145.39
KZ	KUR20	50.64	78.37	48.33	145.39
KZ	KURK	50.72	78.37	48.33	145.39
KZ	MKAR	50.64	78.37	48.23	145.31

Table 3. Information on the stations selected for the 2018 earthquake and the SdP conversion points at the 660-km discontinuity.

Network code	Station code	Latitude (°N)	Longitude (°E)	Conversion point latitude (°N)	Conversion point longitude (°E)
KN	CHM	42.99	74.75	48.06	145.56
KN	ULHL	42.25	76.24	48.04	145.53
KN	USP	43.27	74.50	48.07	145.56
KR	BOOM	42.49	75.94	48.04	145.54
KZ	PDGK	43.33	79.48	48.04	145.49

quakes and stations is presented in Figure 1. We used the S-to-P conversion wave (SdP), a downgoing S wave converting into a P wave at a seismic discontinuity (Figure 1c), such as the 660-km discontinuity below the focus of earthquakes, to characterize the velocity structure across the discontinuity (e.g., Niu FL and Kawakatsu, 1995; Zang SX et al., 2006; Li J et al., 2008, 2023; Zhou YZ et al., 2012; Li J and Yuen, 2014; Yang ZT and He XB, 2015; He XB and Zheng YX, 2018; Yuan Y et al., 2021; He XB, 2022; Cui QH et al., 2018, 2023). The advantage of this approach is that it minimizes the effects introduced by mantle heterogeneities by considering the differential travel times of the SdP versus the P wave because they share similar ray paths defined by the source and receiver (e.g., Wang LM and He XB, 2020). The similarity in ray paths leads to a nearly identical (slightly lower) slowness of the SdP compared with the direct P wave. Vespagram calculations can determine the relative slowness via an *N*th ($N = 4$) root slant stack algorithm (e.g., Zang SX et al., 2006; Hu JF and He XB, 2019).

Before determining the S-to-P conversion depth, we used the differential travel times to reconstrain the focal depths (Figure 2), which reduced the uncertainties on the conversion depths introduced by the errors of the focal depths. We then applied a two-pass, two-pole Butterworth bandpass filter with 0.05 and 0.5 Hz corner frequencies to the vertical component data (e.g., Wang LM and He XB, 2020). Note that the instrumental responses were also removed to yield the velocity seismograms. The record sections comprising the P and SdP waves were aligned along the direct P wave and plotted as a function of the epicentral distance (Figures 3a and 3c). The data show the notably prominent arrivals at ~25 s after the direct P wave, identified as the S-to-P conversion at the 660-km discontinuity and named S660P. The arrivals, clearly shown on the vespagrams (Figures 3b and 3d), were also predicted by the IASP91 model (Kennett and Engdahl, 1991), in which the S660P was slightly slower than that of the direct P wave by 0.05 s/deg. High-quality seismograms offer a rare opportunity to conduct waveform modeling because the arrival time information of S660P has often been extracted by energy stacking to estimate the depth of the 660-km discontinuity (e.g., Li J et al., 2008; Cui QH et al., 2023; Hao G, 2023). Still, the use of waveforms is often minimal because of contamination by noises.

2.2 Validation of S660P Waves

To further identify the second arrival after P as the S-to-P conversion wave, the record sections were rotated to the *LQT* coordinate system (Figure 4). The *L* component showed a large amplitude, and the *Q* and *T* components showed weak signals. This behavior helped validate that the arrivals after P were S-to-P conversion waves.

Before conducting a series of modelings, we compared the simulated waveforms based on the IASP91 model by using two different algorithms, normal-mode summation versus propagation matrix

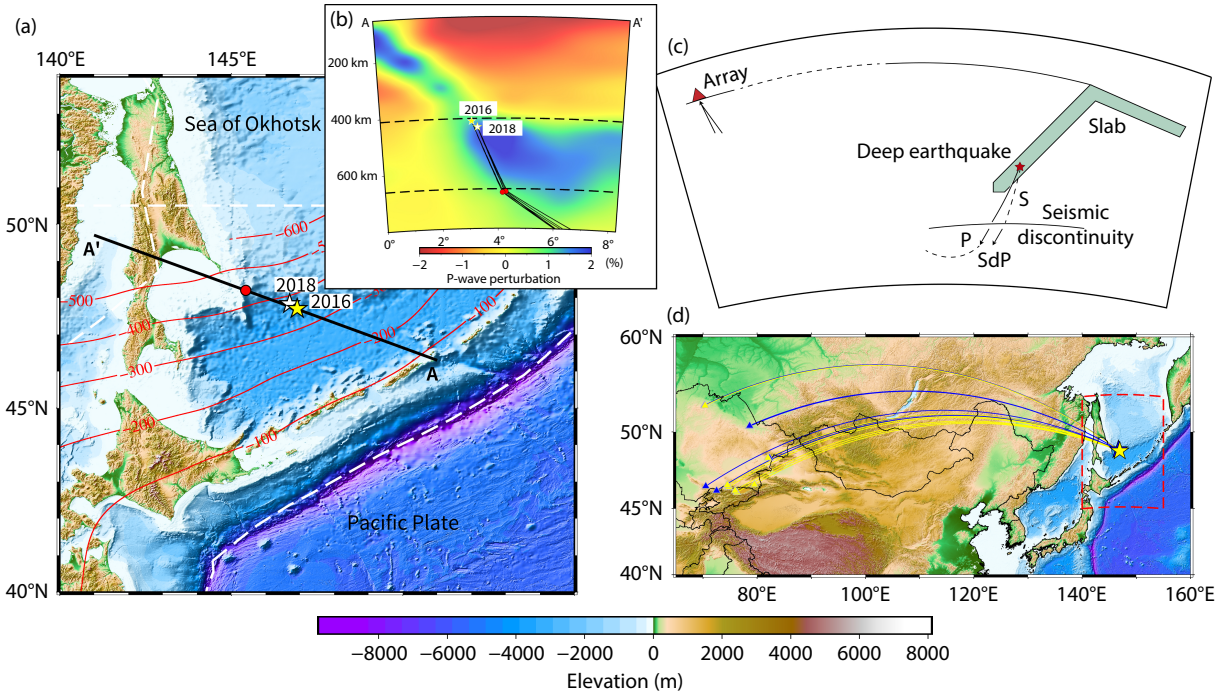

Figure 1. (a) Map showing tectonic settings of the study region. The red lines denote the depth contours of the upper boundaries of slabs. The two events are indicated by a white (the 2018 event) and yellow (the 2016 event) star, respectively. The red dot shows the S-to-P conversion point at the 660-km depth. (b) A vertical cross-section showing the V_p perturbation along the A–A′ profile given by the TX2019 model (Lu G et al., 2019). The black dashed lines denote the S-to-P ray paths at the source side calculated via the TauP Toolkit (Crotwell et al., 1999) based on the IASP91 model (Kennett and Engdahl, 1991). (c) A schematic plot depicting the ray paths for both P and S-to-P (SdP). (d) Map showing the great circle paths, indicated by lines, connecting the two earthquakes and the stations, in which blue corresponds to the 2018 event and yellow corresponds to the 2016 event.

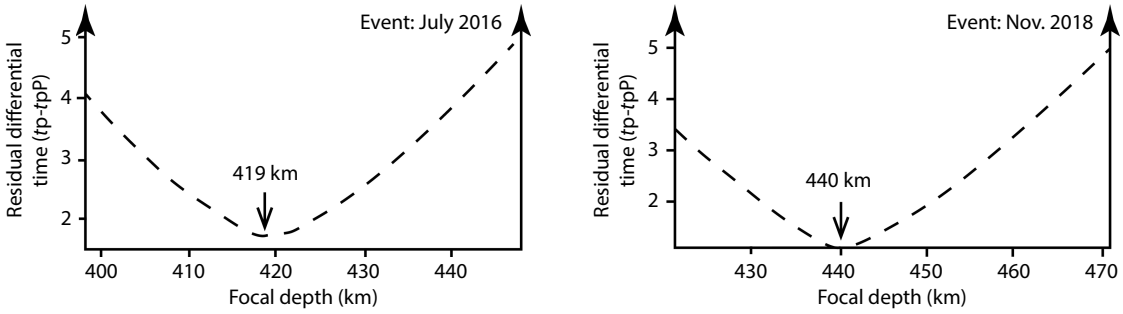

Figure 2. Focal depths reconstrained by incorporating information on differential P and pP travel times for the two events used in this study.

(Wang RJ, 1999). The calculated seismograms showed remarkable similarity (Figure 5), reflecting the excellent reliability of the simulations. Note that we used only the propagation matrix-based algorithm software Qseis (Wang RJ, 1999) to conduct the following simulations. To examine the nature of the S660P wave further, we filtered the downgoing SV waves for the simulations according to the IASP91 model (Kennett and Engdahl, 1991), and the synthetic seismograms showed the vanishment of the S660P wave (Figure 6). This scenario also supports the observed later arrivals after P, very likely as S-to-P converted waves at the 660-km discontinuity. As such, different lines of evidence validated that the arrivals after P were S660P waves (Figure 3).

2.3 Model Construction and Waveform Modeling

The observed S660P waves exhibited high-quality waveforms that could be readily identified without stacking processes (Figure 3). This provided an opportunity to constrain the velocity structure across the 660-km discontinuity below the focus of earthquakes by conducting waveform modeling. We used the trial-and-error method to search for the best model to explain the data. In other words, we conducted waveform modeling based on a suite of velocity models and compared each synthetic waveform with the observed S660P waveform. We evaluated the waveform similarity between the synthetic waveforms and the data by calculating the cross-correlation coefficient (CC). More important, the S660P wave was normalized relative to the S wave. This process minimized the effects of the source radiation pattern because they shared similar energy when excited from the source.

The critical process of the trial-and-error method was to build velocity models for examination. Before modeling the S660P

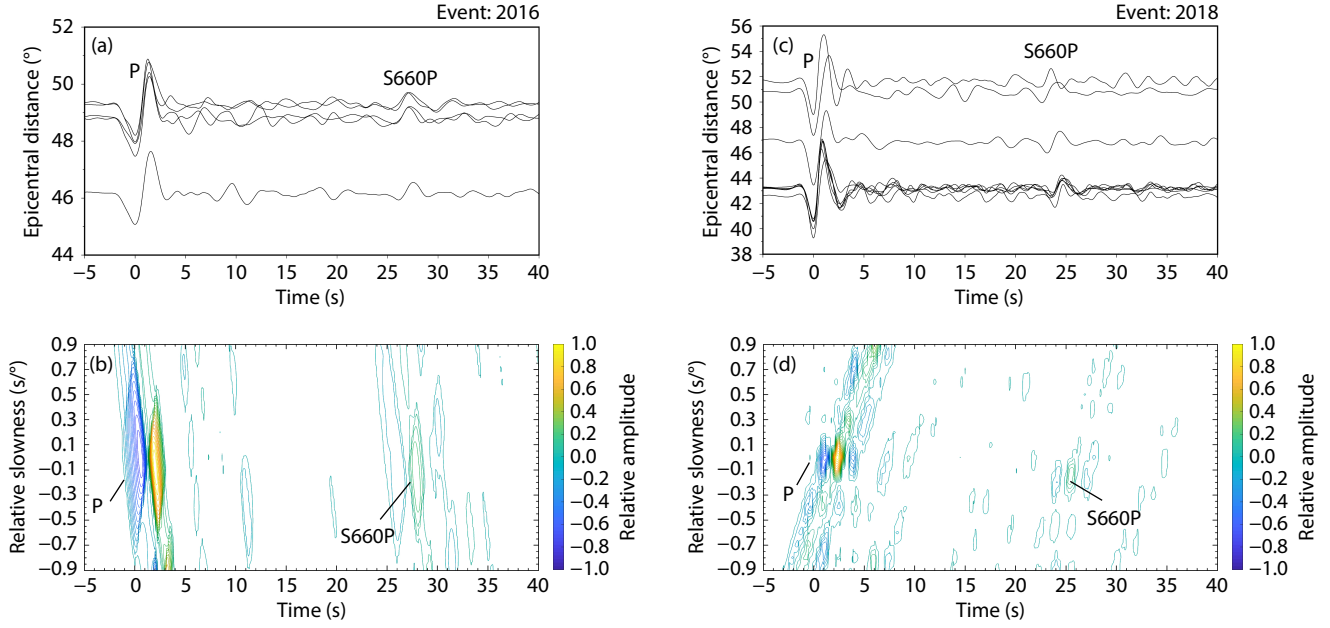

Figure 3. The record sections used in this study (a, c) comprising velocity seismograms and the corresponding data's fourth root vespagrams (b, d). The direct P wave and later arriving S660P are marked.

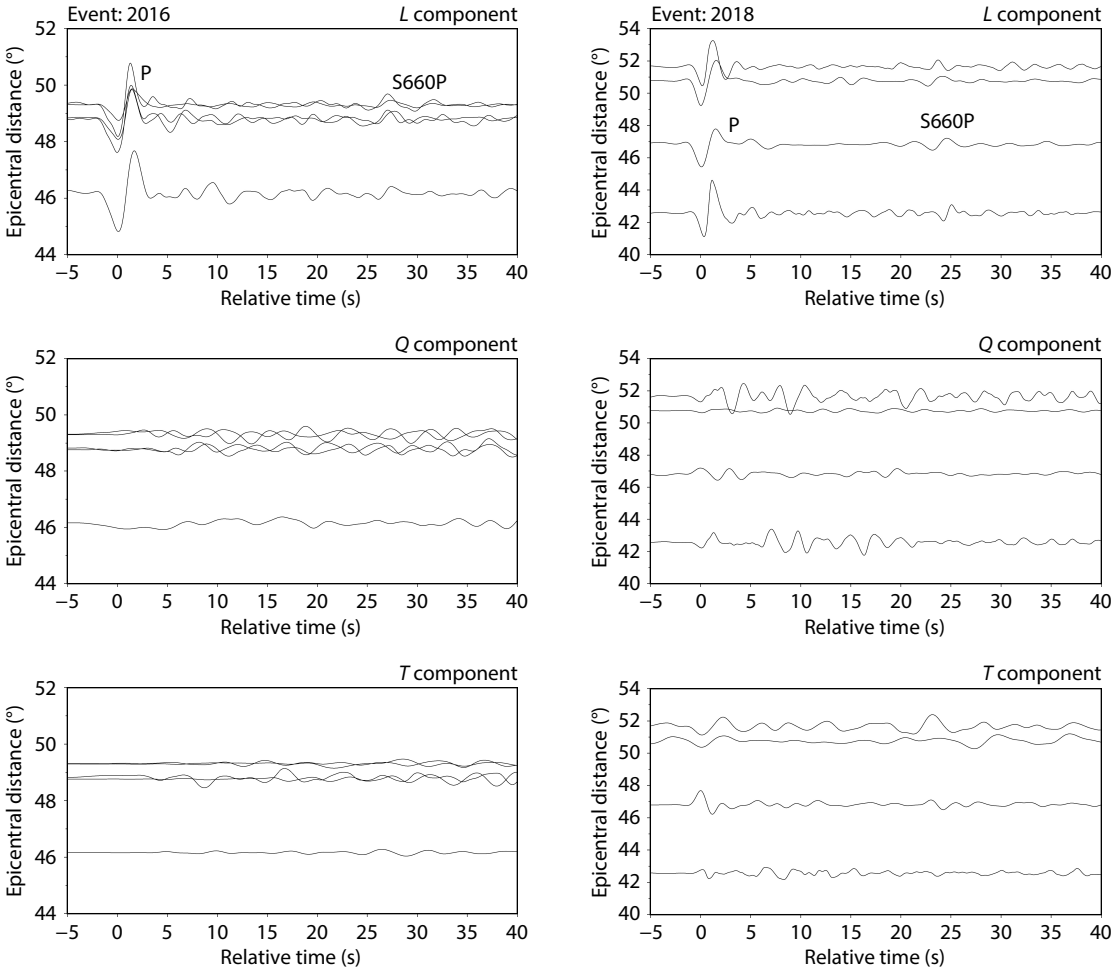

Figure 4. The record sections for the two events in the *LQT* coordinate system. The left column shows the seismograms for the 2016 event, whereas the right column is for the 2018 event.

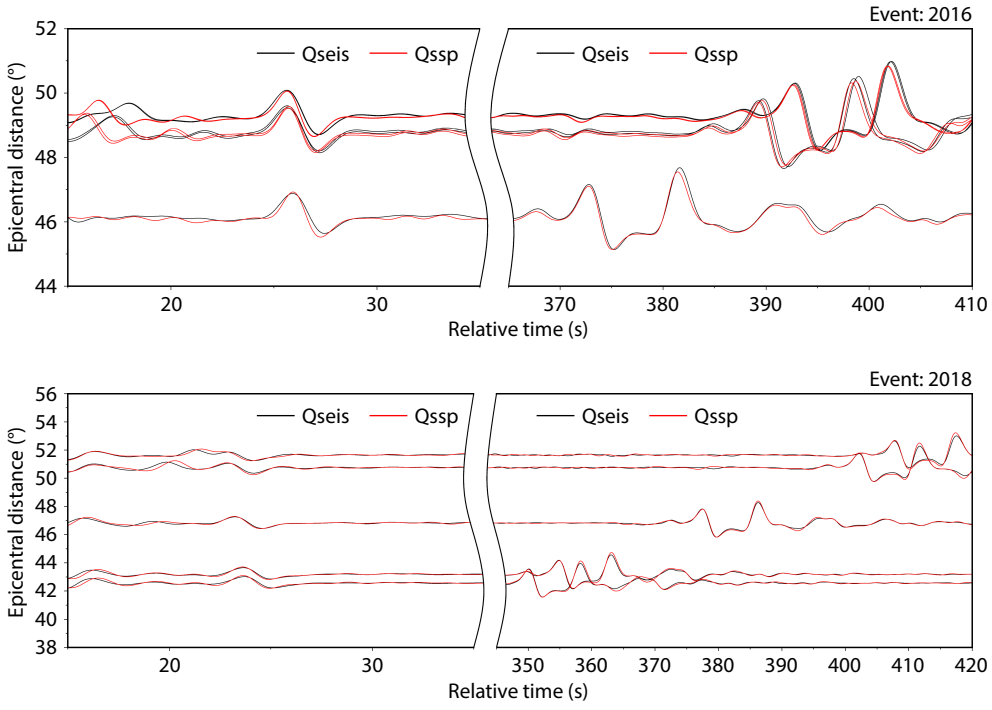

Figure 5. Comparisons of synthetic waveforms in the vertical component calculated by two software programs (Qseis and Qssp). Qseis is based on the propagation matrix algorithm, whereas Qssp is based on the normal-mode summation algorithm. The left column shows the seismograms comprising S660P waveforms, and the right column shows the S wave and its coda.

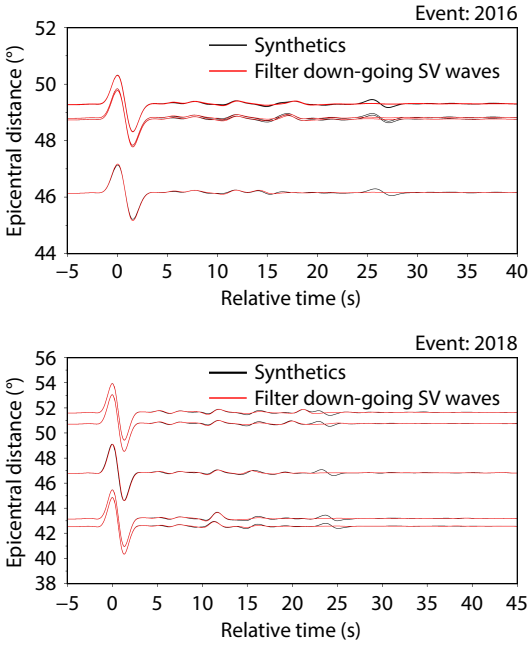

Figure 6. Comparison between synthetic seismograms calculated for the full wavefields (black lines) versus the filtered downgoing SV waves (red lines). A remarkable difference in the arrival of S660P was observed, in which seismograms for the filtered downgoing SV waves showed no S660P waves.

waveforms, we determined the S-to-P conversion depths by considering the differential travel times between P and S660P (Figure 7). The newly determined depths (672 km and 669 km) for the two S-to-P conversions were slightly deeper than 660 km. The underlying causes for the depression of the phase change-related discontinuity are explored in the discussion in Section 3. The constrained conversion depths were further incorporated into the structural models used for waveform simulations.

In this study, we considered only two types of models. The first was the standard IASP91 model (Kennett and Engdahl, 1991), which excellently represented the velocity structure across the 660-km discontinuity at a global scale. The second was a low-velocity layer (LVL) at the base of the MTZ. As mentioned, we aimed to examine whether basalts accumulated at the base of the MTZ in the study area because many studies have demonstrated that segregated basalts display low-velocity signatures in the MTZ (Kono et al., 2012; Feng JK et al., 2021; Wei W et al., 2021). For the IASP91-based model, we used the newly determined S-to-P conversion depth to replace the 660-km depth, whereas the velocity and density were the same as those of the IASP91 model. For the LVL model, a series of models were constructed by varying the thickness of the LVL from 0 to 15 km in increments of 1 km, whereas the velocity reduction of the LVL in V_p varied from −1% to −10%. The V_p versus V_s ratios and density were the same as those of the IASP91 model. According to the built models, we used Qseis software to conduct the waveform simulations and compare the synthetic waveforms with the data, which is elaborated in the next section. The global centroid-moment tensor solution was used for the source mechanisms, and the source time functions were derived from stacked P waveforms.

3. Results and Discussion

3.1 The Depths of S-to-P Conversions

The newly constrained S-to-P conversions occurred at depths of

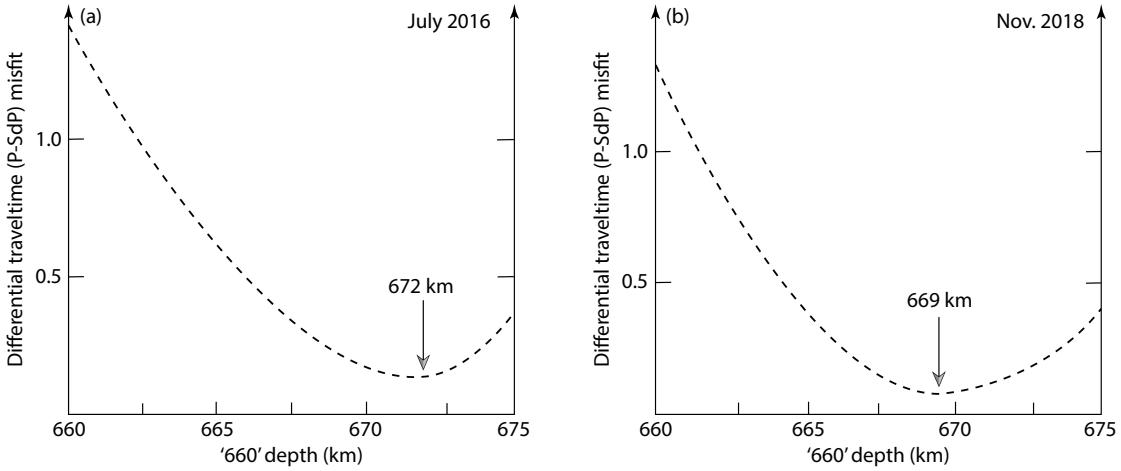

Figure 7. S-to-P conversion depths constrained by differential travel times between P and SdP.

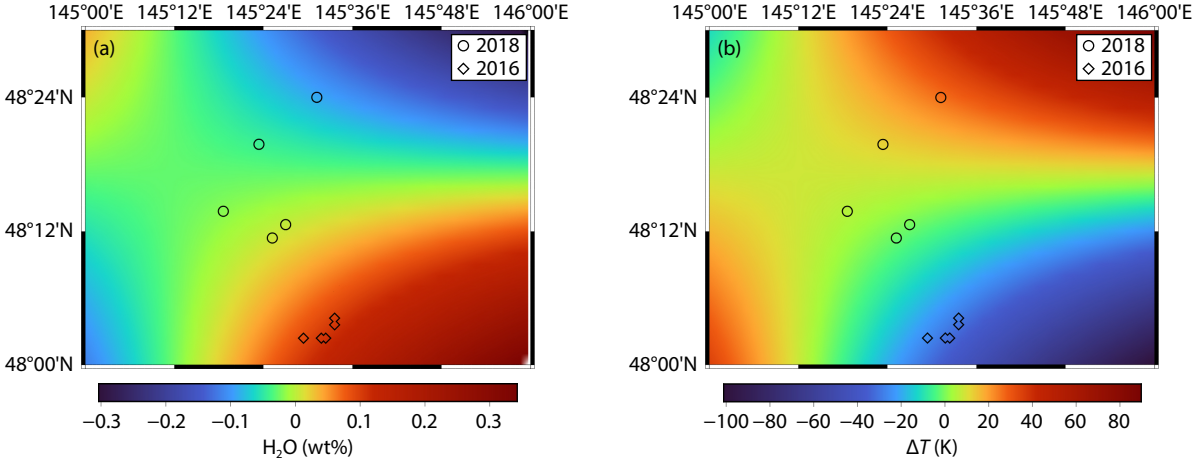

Figure 8. Comparison between the depths of the S-to-P conversion constrained in this study and the model of water and temperature anomalies of the lowermost MTZ given by Wang WZ et al. (2021). For the 2016 event, the S-to-P conversions occurred at a depth of 672 km, clustering in an area with low temperature and water-rich anomalies. In contrast, for the 2018 event, the S-to-P conversions occurred at a depth of 669 km, clustering in an area with no significant temperature and water anomalies.

672 km and 669 km, slightly deeper than 660 km. The gentle depression of depths by 12 km and 9 km could have been caused by a low-temperature anomaly of ~210 K and ~160 K, respectively, according to the negative Clapeyron slope (−2.8 MPa/K) of the transition of ringwoodite to perovskite and magnesiowüstite given by Ito and Takahashi (1989). Note that water also causes depression at a depth of 660 km, as laboratory results have suggested (Litasov et al., 2005). In contrast, it has long been acknowledged that the MTZ is an important water reservoir in the Earth's deep interior, especially underneath subduction zones (e.g., Kuritani et al., 2011; Li J et al., 2013). As such, it leads to ambiguity regarding the relative contribution to the depression of the 660-km discontinuity from temperature and water. If water plays a role, the temperature anomaly would be less than ~210 K and ~160 K. This is probably true because the S-to-P waves abundantly sample the ambient mantle or the margins of the subducting slab rather than the interior of the slab, as shown in the tomographic image (Figure 1b), leading to the gentle temperature anomaly captured by the data.

We compared our observations with a global model (Wang WZ et al., 2021) characterizing the water and temperature anomaly of the lowermost MTZ underneath subduction zones, which was based on seismic tomography and topography of the 660-km discontinuity (Figure 8). In general, our results were consistent with the model of Wang WZ et al. (2021), which explicitly showed the role played by water and temperature in affecting the topography of the 660-km discontinuity. More specifically, for the 2016 event, the S-to-P conversions occurred at a depth of 672 km, clustering in an area with low temperature and water-rich anomalies. In contrast, for the 2018 event, the S-to-P conversions occurred at a depth of 669 km, clustering in an area with no significant temperature and water anomalies.

3.2 The LVL Model

We conducted the simulations based on all the LVL models as described in Section 2.3. Our results showed that the model comparing a 7-km-thick LVL with a V_p reduction of −7% could better explain the data than could other LVL models. Figure 9 presents a comparison between the synthetic waveforms and the data. As mentioned, to minimize the effects of source radiation

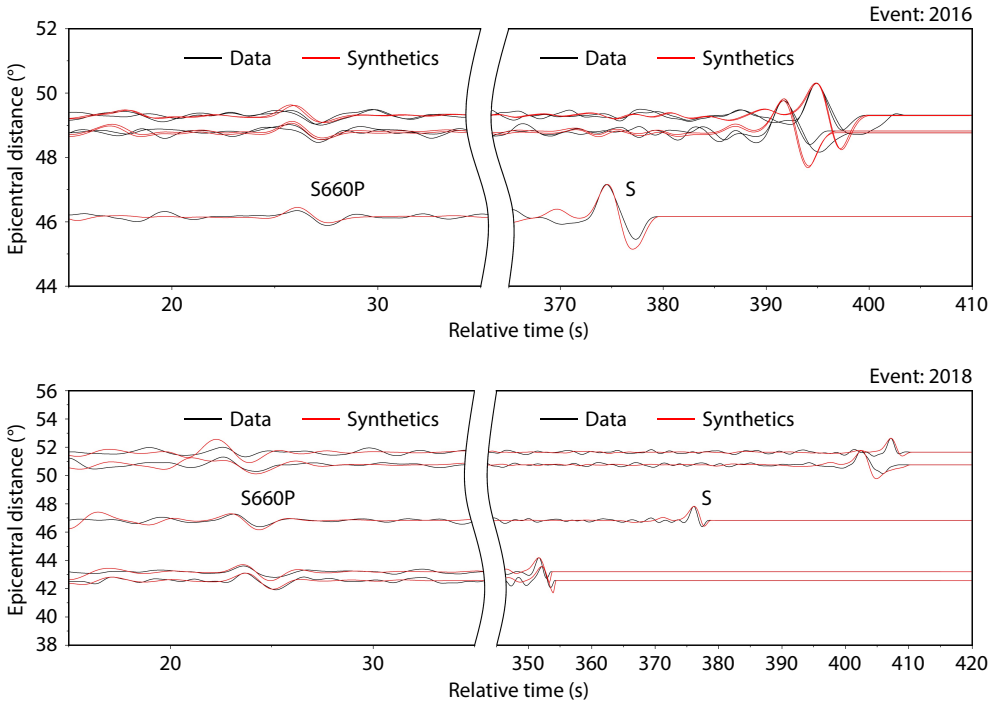

Figure 9. Comparisons between the synthetic waveforms comprising the S660P and the S waves in vertical component, according to the 7-km-thick LVL model and the data. The S wave coda is truncated.

patterns, the seismograms were normalized with respect to the S wave (positive peak-to-zero amplitude). The peak-to-peak amplitude was not used because the negative peak of the synthetic S wave did not fit the data well, particularly for the 2016 event. The cause of the misfit of the S wave's negative peak is explored in Section 3.3. The normalization process is important because it can tell us how the source radiation pattern influenced the simulated waveforms. In general, the synthetic S660P waveforms fit the data adequately. The slowness and amplitude of the S660P could be largely replicated based on the LVL model.

3.3 The IASP91-based Model

The model was similar to the IASP91, except that the 660-km depths were replaced with the newly determined S-to-P conversion depths. In general, the synthetic S660P waveforms also fit the data well (Figure 10). Note that the negative peak of the synthetic S wave did not fit the data either, particularly for the 2016 event. As such, the positive peak-to-zero amplitude of the S wave was used to normalize the seismograms.

To explore possible causes for the misfit between the negative peak of the synthetic S wave and the data, we compared the synthetic S waves with the data in the *T* component (Figure 11). The comparisons showed that the synthetic *T*-component S waves adequately reproduced the data. Therefore, we suspect that some S-to-P conversions and reverberations at shallow structures, such as sediments underneath the stations, probably contaminated the S waveforms in the vertical component. In contrast, the synthetic simulations did not consider such shallow anomalous structures, leading to the misfit between the synthetic waves and the data regarding the negative peaks of the S waves. In any case, we have avoided the potential effects of the misfit by considering the positive peak-to-zero amplitude of S waves as the reference for normalizing seismograms because the positive peak of S waves was not affected by those contamination waves.

3.4 Comparisons Between the LVL and IASP91-based Models

The synthetic waves based on the LVL and IASP91-based models adequately explained the data. To quantify the evaluation of the two models, we calculated the waveform CC between the synthetics and the data. We first used slant-stacking to the SdP waveforms and then calculated the CC between the stacked synthetic waves and the stacked data. Stacking was important because it minimized the noise effect on individual traces. Figures 12–13 (b–c) show the time windows for CC calculation.

The calculated CCs showed that, for both events, the IASP91-based model yielded a greater CC than did the LVL model (0.90 vs. 0.86 and 0.96 vs. 0.94; Figures 12–13). Therefore, the IASP91-based model explained the data better than did the LVL model. Thus, introducing a compositional anomaly layer at the bottom of the MTZ was not required here. In contrast, the 660-km discontinuity was influenced by the temperature or water anomaly atop it, or both, leading to a depressed discontinuity.

3.5 Heterogeneous Distribution of Basalts in the MTZ

Our observations demonstrated that the lowermost MTZ did not contain a basalt layer in the study area, which seemed to conflict with other studies showing a basalt-rich layer at the base of the MTZ (e.g., Bissig et al., 2022) underneath subduction zones. We proposed a conceptual model to reconcile our observations with other results by introducing basalts heterogeneously distributed in the MTZ (Figure 14). More specifically, basalts likely prefer to

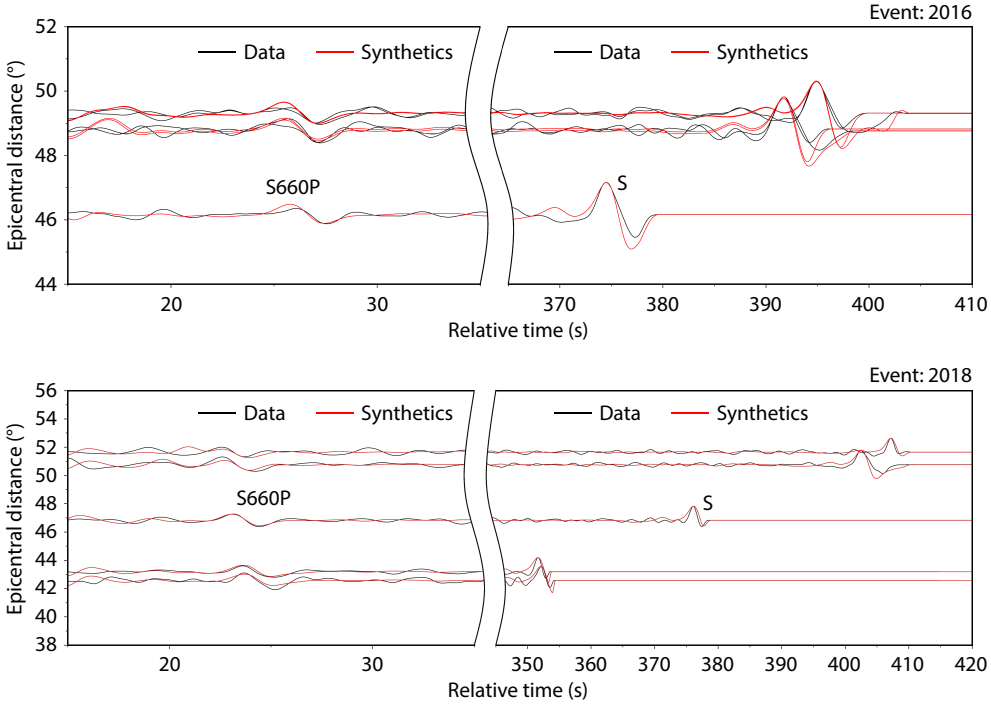

Figure 10. Comparisons between the synthetic waveforms comprising the S660P and the S waves, according to the IASP91-based model and the data. The S wave coda is truncated.

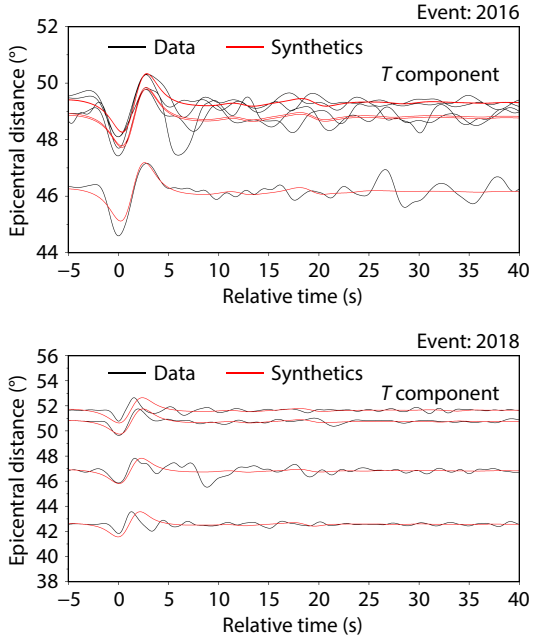

Figure 11. Comparisons between the synthetic seismograms comprising the S waves and the data in the *T* component.

segregate and accumulate in areas on the continent-ward side of a subducting slab at the base of the MTZ. This conceptual model is compatible with the model of Bissig et al. (2022), who used waveform triplications to characterize the structure at the base of the MTZ, sampling the areas between the earthquakes and continental stations (i.e., on the continent-ward side of a subducting slab). In contrast, the areas at the trenchward side of a subducting slab at the base of the MTZ would be poor in basalts or free of basalts because these areas would be close to the subducting oceanic mantle lithosphere rather than the oceanic crust. Our S-to-P waves here happened to sample such a basalt-poor area. In the Izu-Bonin subduction zone, S-to-P waves were sampled in a similar basalt-poor area at the base of the MTZ at the trenchward side of a subducting slab (Wang LM and He XB, 2020), which helped strengthen our model accordingly. Meanwhile, our results favored a sporadic, rather than ubiquitous, accumulation of basalts at the base of the MTZ. In addition, after the segregation and accumulation of basalts, a subsequent series of dynamic processes probably gradually led to compositional homogenization in the MTZ. However, our observations preferred a heterogeneous, most likely far from homogeneous, MTZ. This scenario aligns with the model arguing for a poorly mixed MTZ proposed by Waszek et al. (2021).

3.6 Possible Reservoirs of Basalts

The prerequisite for basalts to segregate and accumulate in the MTZ is separation from the accompanying mantle lithosphere. This process is likely possible because crustal and mantle components of the subducted oceanic lithosphere have distinct densities and viscosities (Karato, 1997). At the same time, a weak serpentinite layer within the subducted oceanic lithosphere could promote decoupling between the oceanic crust and underlying lithosphere (Lee and Chen WP, 2007). Mechanical stirring in the deep mantle (Stixrude and Lithgow-Bertellonic, 2012) and slab–MTZ interactions (Karato, 1997) could help basalts detach from their underlying lithosphere. An accumulation of basalts at the base of the MTZ is also feasible, as supported by numerical experiments (Yan J et al., 2020; Li MM, 2021). If the MTZ represents one of the basalt reservoirs, other important reservoirs could be the mid-mantle (e.g., Bentham and Rost, 2014; Waszek et al., 2018; Kaneshima, 2019)

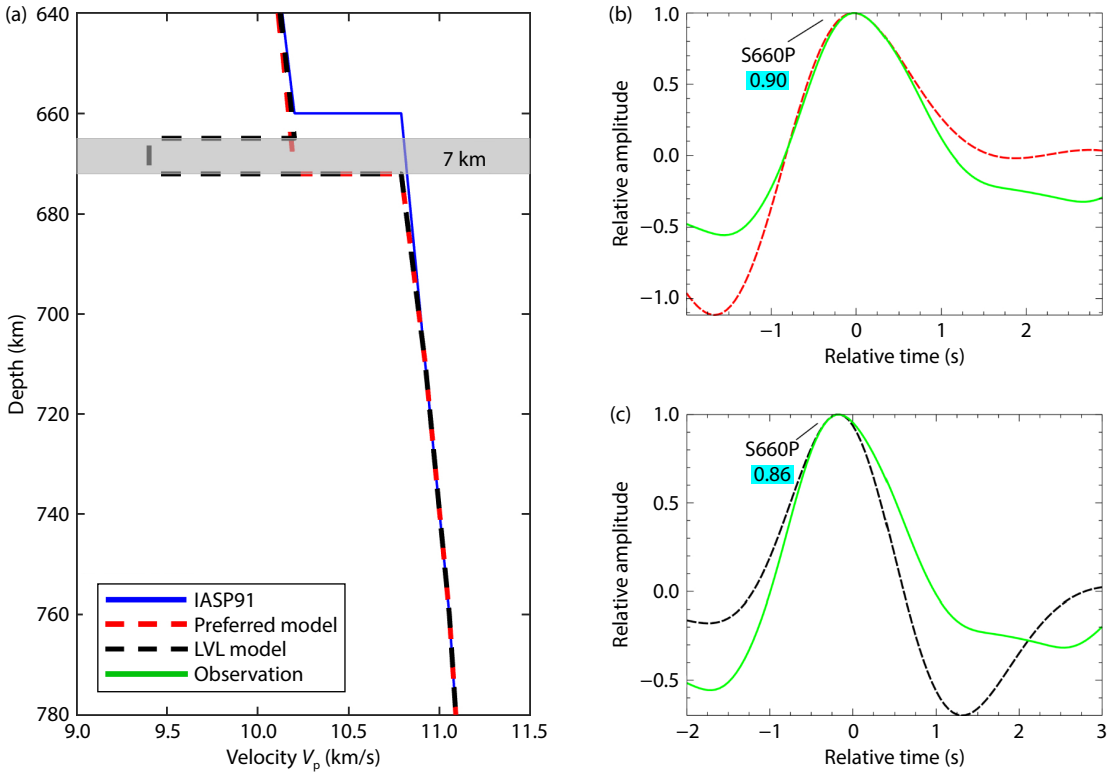

Figure 12. Comparisons between the LVL and IASP91-based model for the 2016 event. (a) Velocity profiles for the IASP91 model, the LVL model, and the IASP91-based model (i.e., the preferred model). (b, c) Comparison of the SdP (slant-stacked waveform, green line) and the synthetic waveforms (IASP91-based model, dashed red line; LVL model, dashed black line; data, green line). The waveform CCs for both phases (0.90 vs. 0.86) are marked.

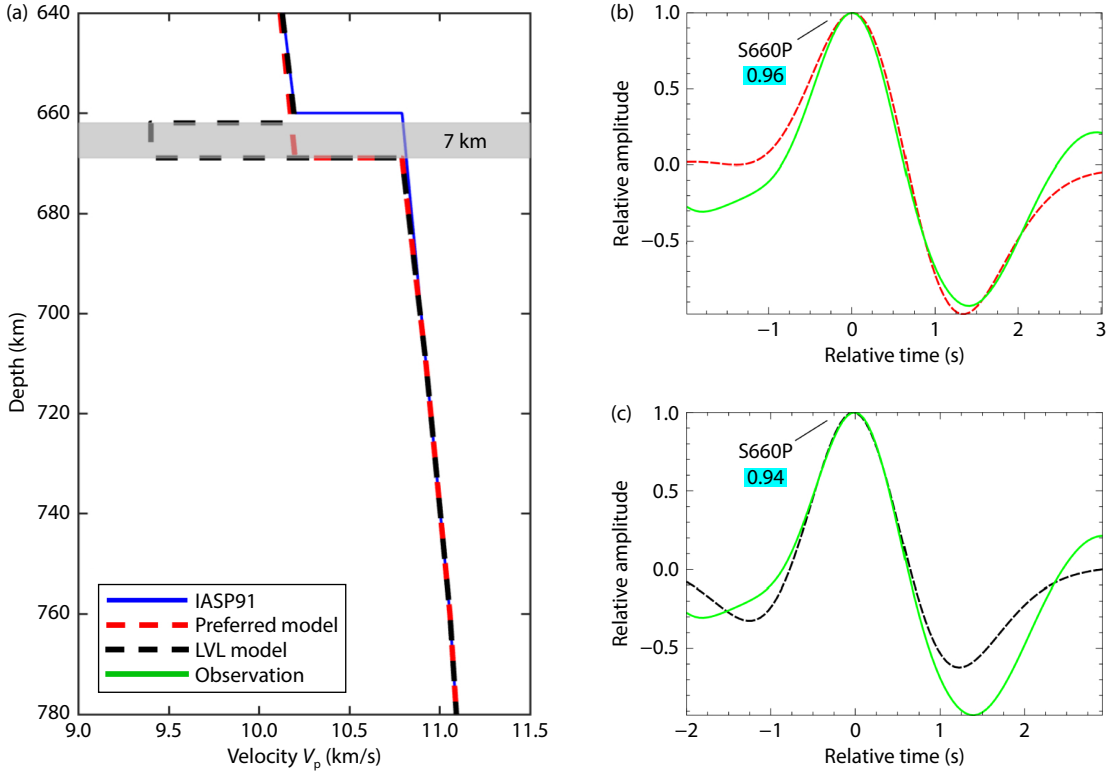

Figure 13. The same as Figure 12, except for the 2018 event.

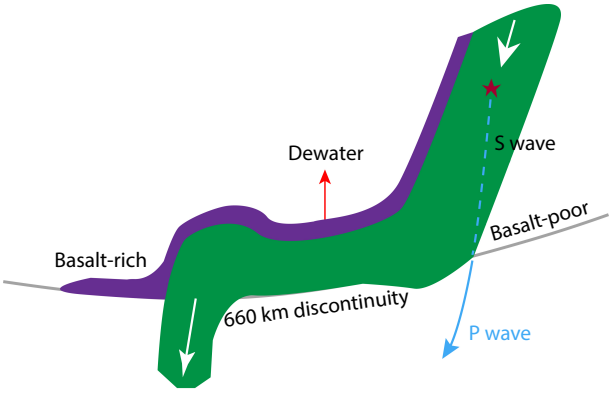

Figure 14. Schematic model illustrating the heterogenous distribution of basalts associated with basalt segregation and accumulation at the base of the MTZ. The area on the continent-ward side of a subducting slab, near the oceanic crust (in purple), is more likely rich in basalts, whereas the area on the trench-ward side of a subducting slab, near the mantle lithosphere (in green) is preferentially rich in harzburgite but poor in basalts. The S-to-P waves in this study happen to sample the basalt-poor area as seen by the tomographic image (Figure 1b).

and the bottom of the mantle (e.g., Li MM and McNamara, 2022; Su YL et al., 2024).

4. Conclusions

In this study, we constrained the velocity structure across the 660-km discontinuity beneath the Sea of Okhotsk by modeling the S660P waveforms. We found that the IASP91 model could adequately replicate the S660P waveforms. At the same time, their arrival times could be explained by temperature or water content anomalies, or both, at the base of the MTZ introduced by the arrival of subducted slabs. Our findings suggest that although slabs have disturbed the MTZ of this area, basalt accumulation and segregation have not occurred. Therefore, we argue for a sporadic, rather than ubiquitous, accumulation and segregation of basalts at the base of the MTZ.

Acknowledgments

We thank Liming Wang and Jinfeng Luo for the data collection and preliminary analysis of this study. The figures were prepared with Generic Mapping Tools (Wessel and Smith, 1991). We are grateful to two anonymous reviewers and the editor for insightful comments that helped us improve the paper. The authors acknowledge support from the National Natural Science Foundation of China (Grant No. 42276049) and the Strategic Priority Research Program of the Chinese Academy of Sciences (Grant No. XDB42020103).

References

Bentham, H. L. M., and Rost, S. (2014). Scattering beneath Western Pacific subduction zones: evidence for oceanic crust in the mid-mantle. *Geophys. J. Int.*, *197*(3), 1627–1641. https://doi.org/10.1093/gji/ggu043

Bina, C. R. (1991). Mantle discontinuities. *Rev. Geophys.*, *29*(S2), 783–793. https://doi.org/10.1002/rog.1991.29.s2.783

Bissig, F., Khan, A., and Giardini, D. (2022). Evidence for basalt enrichment in the mantle transition zone from inversion of triplicated P- and S-waveforms. *Earth Planet. Sci. Lett.*, *580*, 117387. https://doi.org/10.1016/j.epsl.2022.117387

Crotwell, H. P., Owens, T. J., and Ritsema, J. (1999). The TauP Toolkit: flexible seismic travel-time and ray-path utilities. *Seismol. Res. Lett.*, *70*(2), 154–160. https://doi.org/10.1785/gssrl.70.2.154

Cui, Q. H., Li, W. L, Li, G. H., Ma, M. N., Guan, X. Y., and Zhou, Y.Z. (2018). Seismic detection of the X-discontinuity beneath the Ryukyu subduction zone from the SdP conversion phase. *Earth Planet. Phys.*, *2*(3), 208–219. https://doi.org/10.26464/epp2018020

Cui, Q. H., Zhou, Y. Z., Liu, L. J., Gao, Y., Li, G. H., and Zhang, S. F. (2023). The topography of the 660-km discontinuity beneath the Kuril-Kamchatka: implication for morphology and dynamics of the northwestern Pacific slab. *Earth Planet. Sci. Lett.*, *602*, 117967. https://doi.org/10.1016/j.epsl.2022.117967

Feng, J. K., Yao, H. J., Wang, Y., Poli, P., and Mao, Z. (2021). Segregated oceanic crust trapped at the bottom mantle transition zone revealed from ambient noise interferometry. *Nat. Commun.*, *12*(1), 2531. https://doi.org/10.1038/s41467-021-22853-2

Foulger, G. R. (2012). Are 'hot spots' hot spots?. *J. Geodyn.*, *58*, 1–28. https://doi.org/10.1016/j.jog.2011.12.003

Goes, S., Yu, C. Q., Ballmer, M. D., Yan, J., and van der Hilst, R. D. (2022). Compositional heterogeneity in the mantle transition zone. *Nat. Rev. Earth Environ.*, *3*(8), 533–550. https://doi.org/10.1038/s43017-022-00312-w

Hao, G. (2023). Topography of the 660-km discontinuity within the Izu-Bonin subduction zone and evidence of slab penetration near the Bonin Super Deep Earthquake (~680 km). *Earthq. Sci.*, *36*(6), 458–476. https://doi.org/10.1016/j.eqs.2023.06.001

He, X. B., and Zheng, Y. X. (2018). S-to-P conversions from mid-mantle slow scatterers in slab regions: observations of deep/stagnated oceanic crust?. *Pure Appl. Geophys.*, *175*(6), 2045–2055. https://doi.org/10.1007/s00024-017-1763-z

He, X. B. (2022). Small-scale heterogeneity and seismic anisotropy in the mid-mantle: oceanic crust versus meta-stable olivine. *J. Earth Sci.*, *33*(4), 1056–1058. https://doi.org/10.1007/s12583-022-1700-7

Helffrich, G. R., and Wood, B. J. (2001). The Earth's mantle. *Nature*, *412*(6846), 501–507. https://doi.org/10.1038/35087500

Hu, J. F., and He, X. B. (2019). Seismic evidence for a paleoslab in the D″ layer residing adjacent to the southeastern edge of the perm anomaly. *Geochem. Geophys. Geosyst.*, *20*(4), 2040–2052. https://doi.org/10.1029/2019GC008195

Hu, J. S., Liu, L. J., and Zhou, Q. (2018). Reproducing past subduction and mantle flow using high-resolution global convection models. *Earth Planet. Phys.*, *2*(3), 189–207. https://doi.org/10.26464/epp2018019

Ito, E., and Takahashi, E. (1989). Postspinel transformations in the system Mg_2SiO_4-Fe_2SiO_4 and some geophysical implications. *J. Geophys. Res.: Solid Earth*, *94*(B8), 10637–10646. https://doi.org/10.1029/JB094iB08p10637

Kaneshima, S. (2019). Seismic scatterers in the lower mantle near subduction zones. *Geophys. J. Int.*, *219*(S1), S2–S20. https://doi.org/10.1093/gji/ggz241

Karato, S. I. (1997). On the separation of crustal component from subducted oceanic lithosphere near the 660 km discontinuity. *Phys. Earth Planet. Inter.*, *99*(1-2), 103–111. https://doi.org/10.1016/S0031-9201(96)03198-6

Kennett, B. L. N., and Engdahl, E. R. (1991). Traveltimes for global earthquake location and phase identification. *Geophys. J. Int.*, *105*(2), 429–465. https://doi.org/10.1111/j.1365-246X.1991.tb06724.x

Kono, Y., Irifune, T., Ohfuji, H., Higo, Y., and Funakoshi, K. I. (2012). Sound velocities of MORB and absence of a basaltic layer in the mantle transition region. *Geophys. Res. Lett.*, *39*(24), L24306. https://doi.org/10.1029/2012gl054009

Kuritani, T., Ohtani, E., and Kimura, J. I. (2011). Intensive hydration of the mantle transition zone beneath China caused by ancient slab stagnation. *Nat. Geosci.*, *4*(10), 713–716. https://doi.org/10.1038/ngeo1250

Lee, C.-T. A., and Chen, W.-P. (2007). Possible density segregation of subducted oceanic lithosphere along a weak serpentinite layer and implications for compositional stratification of the Earth's mantle. *Earth Planet. Sci. Lett.*, *255*(3-4), 357–366. https://doi.org/10.1016/j.epsl.2006.12.022

Li, J., Chen, Q. F., Vanacore, E., and Niu, F. L. (2008). Topography of the 660-km discontinuity beneath northeast China: implications for a retrograde motion of the subducting Pacific slab. *Geophys. Res. Lett.*, *35*(1), L01302. https://doi.org/10.1029/2007gl031658

Li, J., Wang, X., Wang, X. J., and Yuen, D. A. (2013). P and SH velocity structure in the upper mantle beneath Northeast China: evidence for a stagnant slab in hydrous mantle transition zone. *Earth Planet. Sci. Lett.*, *367*, 71–81. https://doi.org/10.1016/j.epsl.2013.02.026

Li, J., and Yuen, D. A. (2014). Mid-mantle heterogeneities associated with Izanagi plate: implications for regional mantle viscosity. *Earth Planet. Sci. Lett.*, *385*, 137–144. https://doi.org/10.1016/j.epsl.2013.10.042

Li, J., Chen, S. D., He, X. B., Wang, W., and Yang, F. (2023). Mid-lower mantle scatterers: detection methods, research progress and prospect. *Rev. Geophys. Planet. Phys. (in Chinese)*, *54*(3), 339–354. https://doi.org/10.19975/j.dqyxx.2022-039

Li, M. M. (2021). The cycling of subducted oceanic crust in the Earth's deep mantle. In H. Marquardt, et al. (Eds.), *Mantle Convection and Surface Expressions* (pp. 303–328). Washington, DC: American Geophysical Union. https://doi.org/10.1002/9781119528609.ch12

Li, M. M., and McNamara, A. K. (2022). Evolving morphology of crustal accumulations in Earth's lowermost mantle. *Earth Planet. Sci. Lett.*, *577*, 117265. https://doi.org/10.1016/j.epsl.2021.117265

Litasov, K. D., Ohtani, E., Sano, A., Suzuki, A., and Funakoshi, K. (2005). Wet subduction versus cold subduction. *Geophys. Res. Lett.*, *32*(13), L13312. https://doi.org/10.1029/2005gl022921

Lu, C., Grand, S. P., Lai, H. Y., and Garnero, E. J. (2019). TX2019slab: a new *P* and *S* tomography model incorporating subducting slabs. *J. Geophys. Res.: Solid Earth*, *124*(11), 11549–11567. https://doi.org/10.1029/2019jb017448

Morgan, J. P., and Shearer, P. M. (1993). Seismic constraints on mantle flow and topography of the 660-km discontinuity: evidence for whole-mantle convection. *Nature*, *365*(6446), 506–511. https://doi.org/10.1038/365506a0

Niu, F. L., and Kawakatsu, H. (1995). Direct evidence for the undulation of the 660-km discontinuity beneath Tonga: comparison of Japan and California array data. *Geophys. Res. Lett.*, *22*(5), 531–534. https://doi.org/10.1029/94gl03332

Papanagnou, I., Schuberth, B. S. A., and Thomas, C. (2023). Geodynamic predictions of seismic structure and discontinuity topography of the mantle transition zone. *Geophys. J. Int.*, *234*(1), 355–378. https://doi.org/10.1093/gji/ggac478

Shearer, P. M. (1995). Seismic studies of the upper mantle and transition zone. *Rev. Geophys.*, *33*(S1), 321–324. https://doi.org/10.1029/95RG00186

Shen, X. Z., Yuan, X. H., and Li, X. Q. (2014). A ubiquitous low-velocity layer at the base of the mantle transition zone. *Geophys. Res. Lett.*, *41*(3), 836–842. https://doi.org/10.1002/2013gl058918

Shen, Y., and Blum, J. (2003). Seismic evidence for accumulated oceanic crust above the 660-km discontinuity beneath southern Africa. *Geophys. Res. Lett.*, *30*(18), 1925. https://doi.org/10.1029/2003gl017991

Smyth, J. R., and Frost, D. J. (2002). The effect of water on the 410-km discontinuity: an experimental study. *Geophys. Res. Lett.*, *29*(10), 1485. https://doi.org/10.1029/2001gl014418

Stixrude, L., and Lithgow-Bertelloni, C. (2012). Geophysics of chemical heterogeneity in the mantle. *Annu. Rev. Earth Planet. Sci.*, *40*(1), 569–595. https://doi.org/10.1146/annurev.earth.36.031207.124244

Su, Y. L., Ni, S. D., Zhang, B. L., Chen, Y. L., Wu, W. B., Li, M. M., Sun, H. P., Hou, M. Q., Cui, X. M., and Sun, D. Y. (2024). Detections of ultralow velocity zones in high-velocity lowermost mantle linked to subducted slabs. *Nat. Geosci.*, *17*(4), 332–339. https://doi.org/10.1038/s41561-024-01394-5

Tauzin, B., Waszek, L., Ballmer, M. D., Afonso, J. C., and Bodin, T. (2022). Basaltic reservoirs in the Earth's mantle transition zone. *Proc. Natl. Acad. Sci. USA*, *119*(48), e2209399119. https://doi.org/10.1073/pnas.2209399119

Taylor, G., Thompson, D. A., Cornwell, D., and Rost, S. (2019). Interaction of the Cyprus/Tethys slab with the mantle transition zone beneath Anatolia. *Geophys. J. Int.*, *216*(3), 1665–1674. https://doi.org/10.1093/gji/ggy514

Wang, J. C., Gu, Y. J., and Schmerr, N. (2023). Global variability of density contrast across the 660-km discontinuity. *Geophys. Res. Lett.*, *50*(4), e2022GL101213. https://doi.org/10.1029/2022gl101213

Wang, L. M., and He, X. B. (2020). Sharpness of the paired 660-km discontinuity beneath the Izu-Bonin area. *Earth Planet. Phys.*, *4*(6), 627–638. https://doi.org/10.26464/epp2020067

Wang, R. J. (1999). A simple orthonormalization method for stable and efficient computation of Green's functions. *Bull. Seismol. Soc. Am.*, *89*(3), 733–741. https://doi.org/10.1785/BSSA0890030733

Wang, W. Z., Zhang, H., Brodholt, J. P., and Wu, Z. Q. (2021). Elasticity of hydrous ringwoodite at mantle conditions: implication for water distribution in the lowermost mantle transition zone. *Earth Planet. Sci. Lett.*, *554*, 116626. https://doi.org/10.1016/j.epsl.2020.116626

Waszek, L., Schmerr, N. C., and Ballmer, M. D. (2018). Global observations of reflectors in the mid-mantle with implications for mantle structure and dynamics. *Nat. Commun.*, *9*(1), 385. https://doi.org/10.1038/s41467-017-02709-4

Waszek, L., Tauzin, B., Schmerr, N. C., Ballmer, M. D., and Afonso, J. C. (2021). A poorly mixed mantle transition zone and its thermal state inferred from seismic waves. *Nat. Geosci.*, *14*(12), 949–955. https://doi.org/10.1038/s41561-021-00850-w

Wei, W., Mao, Z., Sun, N. Y., Sun, D. Y., and Tkachev, S. N. (2021). High pressure-temperature single-crystal elasticity of grossular: implications for the low-velocity layer in the bottom transition zone. *Geophys. Res. Lett.*, *48*(9), e2021GL093540. https://doi.org/10.1029/2021gl093540

Wessel, P., and Smith, W. H. F. (1991). Free software helps map and display data. *Eos Trans. Am. Geophys. Union*, *72*(41), 441–446. https://doi.org/10.1029/90EO00319

Wood, B. J. (1995). The effect of H_2O on the 410-kilometer seismic discontinuity. *Science*, *268*(5207), 74–76. https://doi.org/10.1126/science.268.5207.74

Yan, J., Ballmer, M. D., and Tackley, P. J. (2020). The evolution and distribution of recycled oceanic crust in the Earth's mantle: insight from geodynamic models. *Earth Planet. Sci. Lett.*, *537*, 116171. https://doi.org/10.1016/j.epsl.2020.116171

Yang, Z. T., and He, X. B. (2015). Oceanic crust in the mid-mantle beneath west-central Pacific subduction zones: evidence from *S* to *P* converted waveforms. *Geophys. J. Int.*, *203*(1), 541–547. https://doi.org/10.1093/gji/ggv314

Yu, C. Q., Goes, S., Day, E. A., and van der Hilst, R. D. (2023). Seismic evidence for global basalt accumulation in the mantle transition zone. *Sci. Adv.*, *9*(22), eadg0095. https://doi.org/10.1126/sciadv.adg0095

Yuan, Y., Sun, D., Leng, W., and Wu, Z. (2021). Southeastward dipping mid-mantle heterogeneities beneath the sea of Okhotsk. *Earth Planet. Sci. Lett.*, *573*, 117151. https://doi.org/10.1016/j.epsl.2021.117151

Zang, S. X., Zhou, Y. Z., Ning, J. Y., and Wei, R. Q. (2006). Multiple discontinuities near 660 km beneath Tonga area. *Geophys. Res. Lett.*, *33*(20), L20312. https://doi.org/10.1029/2006gl027262

Zhou, Y. Z., Yu, X. W., Yang, H., and Zang, S. X. (2012). Multiplicity of the 660-km discontinuity beneath the Izu-Bonin area. *Phys. Earth Planet. Inter., 198–199*, 51–60. https://doi.org/10.1016/j.pepi.2012.03.003